AIAA 2005-4531

Hydrodynamic Instability of the Bidirectional Vortex

E. M. Abu-Irshaid and J. Majdalani
Advanced Theoretical Research Center
University of Tennessee Space Institute
Tullahoma, TN 37388

G. Casalis
ONERA-CERT
31055 Toulouse Cedex 4, France

41st AIAA/ASME/SAE/ASEE Joint Propulsion Conference and Exhibit
10–13 July 2005
Tucson, AZ

41st AIAA/ASME/SAE/ASEE Joint Propulsion Conference and Exhibit
10-13 July 2005, Tucson, Arizona

AIAA 2005-4531

Hydrodynamic Instability of the Bidirectional Vortex

Esam M. Abu-Irshaid* and Joseph Majdalani†
University of Tennessee Space Institute, Tullahoma, TN 37388

and

Grégoire Casalis‡
ONERA-CERT, 2 Avenue Ed. Belin, B.P. 4025, 31055 Toulouse Cedex 4, France

This work examines the hydrodynamic instability of the bidirectional vortex that is used to describe the flowfield engendered in NASA's cold-wall liquid-liquid vortex chamber. The mean flow profile to be analyzed is based on the analytical solution obtained recently by Vyas, Majdalani and Chiaverini (Vyas, A. B., Majdalani, J., and Chiaverini, M. J., "The Bidirectional Vortex. Part 2: Viscous Core Corrections," AIAA Paper 2003-5053, July 2003). To control the numerical accuracy, the Local Non-Parallel (LNP) approach is implemented such that axial, radial and, especially, tangential disturbances are accounted for. Both temporal and spatial stability theories are investigated and compared. At the outset, both time-dependent and spatial amplifications are independently characterized. The known singularity along the chamber axis is removed using Taylor series expansions. The corresponding boundary conditions are connected to the tangential wave number *q* to the extent that three classes of solutions are identified depending on whether *q* is 0, 1, or higher. For each frequency and spatial location, more than one eigenmode is captured. Also, the zeroth tangential mode is found to be the most unstable. Based on the most amplified mode, the range of stable frequencies and aspect ratios are determined for each Reynolds and swirl number. Based on the e^n method for predicting transition to turbulence, the iso-*n* factor is calculated and found to be less than unity, specifically, too small to suggest that breakdown could be instigated. By comparison to the Taylor-Culick profile used in solid rocket motors, the characteristic stability curves associated with the bidirectional vortex are nearly reversed. Here, the most unstable region shifts from the headend to the downstream injection plane as the tangential mode number switches between 0 and 1. Increasing each of the Reynolds number, swirl number, or aspect ratio has a destabilizing effect although no region could be associated with sufficiently large amplification rates.

Nomenclature

a	=	chamber radius
A_i	=	inlet area
b	=	chamber discharge radius
l	=	chamber aspect ratio, L/a
P	=	normalized mean pressure, $\overline{P}/(\rho U_{inj}^2)$
p	=	normalized pressure amplitude, $\overline{p}/(\rho U_{inj}^2)$
$\overline{Q}_i$	=	inlet volumetric flow rate
Q_i	=	normalized volumetric flow rate, $\overline{Q}_i/(U_{inj}a^2) = \sigma^{-1}$
Re	=	injection Reynolds number, $U_{inj}a/\nu$
r	=	normalized radial coordinate, $\overline{r}/a$

*Graduate student and Research Associate, Department of Mechanical, Aerospace and Biomedical Engineering. Member AIAA.
†Jack D. Whitfield Professor of High Speed Flows, Department of Mechanical, Aerospace and Biomedical Engineering. Member AIAA.
‡Research Scientist, Aerodynamics and Energetics Modeling Department, Member AIAA.

S = swirl number, $\pi ab / A_i = \pi\sigma / \sqrt{2}$
u = normalized velocity amplitude $(\overline{u}_r, \overline{u}_z, \overline{u}_\theta)/U_{inj}$
U = normalized mean inflow velocity, $\left(\overline{U}_r, \overline{U}_\theta, \overline{U}_z\right)/U_{inj}$
$\overline{U}_{inj}$ = tangential injection velocity $\overline{Q}_i / A_i$
V = vortex Reynolds number, $Q_i Re(a/L)$
z = normalized axial coordinate, $\overline{z}/a$

β = normalized discharge radius, b/a
κ = inflow parameter, $Q_i/(2\pi l) = (2\pi\sigma l)^{-1}$
ν = kinematic viscosity, μ/ρ
ρ = density
σ = modified swirl number, $Q_i^{-1} = S\sqrt{2}/\pi$

Subscripts
i = inlet property
r = radial component or partial derivative
z = axial component or partial derivative
$\underline{\theta}$ = azimuthal component or partial derivative
= overbars denote dimensional variables
~ = denotes total (instantaneous) quantities
^ = denotes fluctuating quantities

I. Introduction

THIS work is concerned with the hydrodynamic instability of the bidirectional vortex which is used to describe the bulk internal flow motion observed in both NASA's and ORBITEC's cold-wall, liquid-liquid vortex engines.[1-5] The chief distinction between the two engines lies in the positioning of fuel injection, specifically, at the aft section (just upstream of the nozzle) in lieu of the headend, respectively. The bidirectional vortex refers to the mean cyclonic flow profile arising in the presence of strong tangential injection which, in turn, leads to the formation of a pair of co-axial, co-rotating, counter-flowing, annular and cylindrical, outer and inner vortices. Such bipolar, swirling motion is shown to promote higher combustion efficiency (due to increased fuel and oxidizer mixing), reduced thermal loading and, hence, wall thickness (due to internal convective cooling induced by the outer vortex), and reduced overall size and weight (due, in part, to the spiraling, two-pass particle trajectory).[6-8] At the time of this writing, the bidirectional vortex concept is being implemented in the design of four 7,500 lb thrust engines that are meant to be deployed on the Rocketplane XP, a suborbital vehicle scheduled to carry a 900 lb human payload to an altitude of 350,000 ft and safely back to Oklahoma's Spaceport in November 2006.

The idea of applying cyclonic motion to the design of propulsive devices was first introduced in the design of a low-cost, lightweight, high regression, vortex injection hybrid rocket engine (VIHRE).[9,10] The same injection concept was later implemented in the design of a liquid rocket[7] and vortex ramjet engines.[11] The bidirectional vortex was shown to be a possible solution to Euler's equations in 2003 with the advancement of an exact, rotational, incompressible mean flow profile that displayed the essential elements of cyclonic motion in a cylindrical chamber.[1] Being inviscid, its tangential component exhibited a singularity along the chamber axis, a known characteristic of swirl-driven motion (see Bloor and Ingham[12]). The singularity was quickly removed by regularizing the tangential momentum equation in a manner to capture the viscous stresses responsible for the onset of forced vortex behavior in the chamber core.[2] The resulting profile was shown to provide an adequate representation of the flowfield observed in the numerically simulated engine under both cold-flow[4] and reactive chamber conditions.[5]

It is the purpose of this article to study the hydrodynamic instability of the incompressible bidirectional vortex obtained analytically by Vyas, Majdalani and Chiaverini.[2] This will help to assess the critical parameters that may lead to wave growth and potential excursions in chamber pressure and engine thrust. The overall approach is based on the Local Non-Parallel (LNP) technique that involves solving the dispersion equations derived from the three dimensional incompressible Navier-Stokes equations using normal mode decomposition that retains non-parallel disturbances (i.e., both radial and tangential components of pressure and velocity). This approach has been refined by Casalis, Avalon and Pineau[13] who have applied it in investigating the instability of injection-driven flow configurations simulating solid propellant rockets. In the same vein, Casalis and co-workers[13-18] have explored

Culick's and Taylor's rotational, incompressible and inviscid approximations for the flow in cylindrical and slab rocket motors, respectively. Their results were shown to agree fairly well with critical frequencies and axial distances measured experimentally in both porous tubes and channels. These studies have experimented with and compared three general approaches:

- the OSE or Local Parallel approach based on solving the Orr-Sommerfeld Equation (OSE); here, the tangential and radial disturbances are discounted, thus leading to potentially inaccurate results;[19]
- the Local Non-Parallel (LNP) approach in which tangential and radial disturbances are kept; and
- the Parabolized Stability Equations (PSE) described by Herbert[20] and Bertolotti.[21]

Due to the relative simplicity and accuracy of the LNP approach, it will be applied to investigate both temporal and spatial instability characteristics of the bidirectional vortex, giving particular attention to changes in the tangential wave number, the injection Reynolds number, and the swirl parameter. When helpful, results will be compared to the stability characteristics of the Majdalani-Vyas flow model.[22] Being an extended version of the Taylor-Culick profile,[23] this baseline solution has been extensively validated and used in modeling solid and, recently, hybrid rocket motors.

II. Physical and Mathematical Models

This section describes the geometrical model which may be used to represent the bidirectional vortex chamber for which an analytical mean flow solution can be offered as a possible approximation. This is followed by the system of equations appropriate for this model and a description of the hydrodynamic instability theory to be used.

A. Flow Geometry

The actual setting for the vortex engine is illustrated in Fig. 1 side-by-side with the idealized non-reactive model to be investigated. In Fig. 1a, the flowfield is composed of an outer swirling annular region and an inner tubular core to which reactions are confined.[5,7] The outer region (called outer vortex) is formed by the oxidizer stream injected tangentially to the inner circumference; injection occurs at an appreciable swirl number and a small distance above the nozzle entrance plane. Due to the continual buildup in its angular momentum, the oxidizer stream is compelled to spiral around and up the chamber wall, reversing axial direction at the headend, and returning to the nozzle. The inner vortex refers to the near-core region in which the axial velocity is positive. At or near the headend,

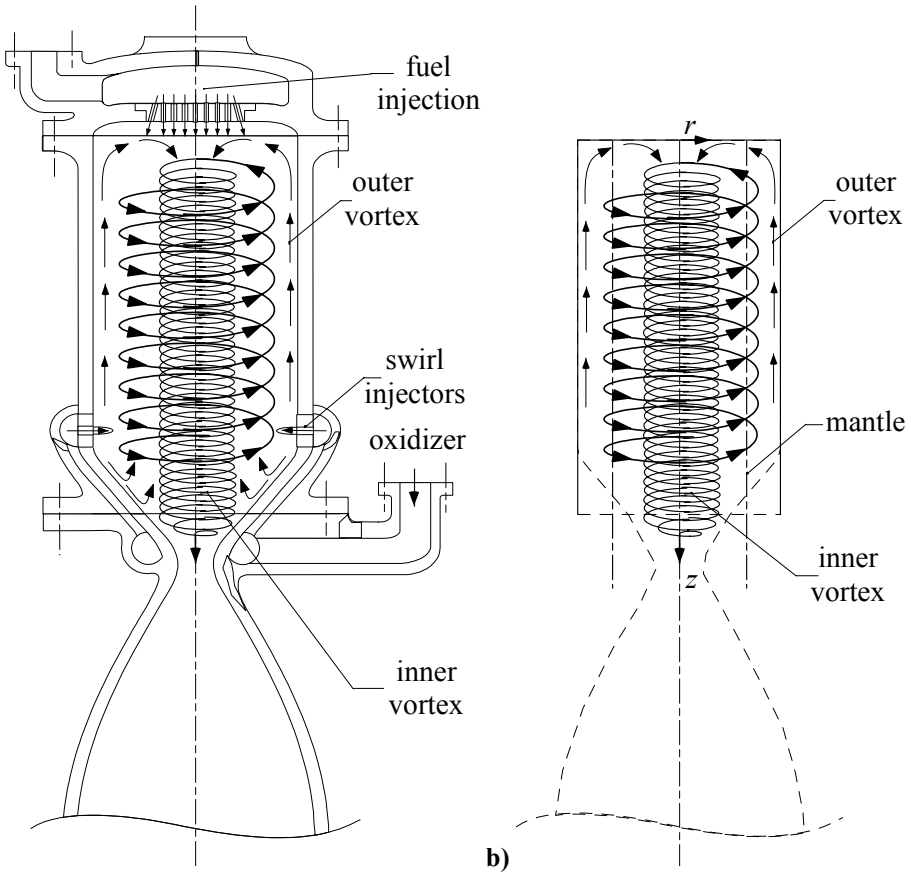

Figure 1. Schematics showing a) the physical prototype and b) the idealized model.

fuel is added. Along the chamber's length, a nearly constant radial flux of oxidizer is exchanged as the flow crosses from outer to inner vortex regions.[1] As the outer vortex denotes the region with negative axial velocity (where motion is toward the headend), a so-called spinning wheel or mantle is formed at the interface separating the outer and inner vortices. In the idealized model shown in Fig. 1b, this rotating but non-translating layer is denoted by the chained line. On the other hand, dashed lines refer to hypothetical surfaces in the actual engine. The idealized chamber has length L and radius a. Other parameters are defined in the Nomenclature. The flow is assumed to be incompressible, inert, single phase, rotational, and nozzleless. Unlike the actual engine in which fuel is injected near the faceplate, the headend in Fig. 1b is impervious. As a result, the mean flow solution, specifically, the one obtained using matched asymptotic expansions,[2] becomes an adequate representation of the bulk flowfield, albeit unable to capture the endwall boundary layers. In Fig. 1b, a polar cylindrical coordinate system is sketched.

B. Equations

Assuming unsteady, rotational, incompressible, single species, nonreactive flow, the continuity and Navier-Stokes equations for the instantaneous flow could be made dimensionless, as usual, and written as

continuity:

$$\frac{\partial \tilde{U}_r}{\partial r}+\frac{\tilde{U}_r}{r}+\frac{1}{r}\frac{\partial \tilde{U}_\theta}{\partial \theta}+\frac{\partial \tilde{U}_z}{\partial z}=0 \tag{1}$$

r-momentum:

$$\frac{\partial \tilde{U}_r}{\partial t}+\tilde{U}_r\frac{\partial \tilde{U}_r}{\partial r}+\frac{\tilde{U}_\theta}{r}\frac{\partial \tilde{U}_r}{\partial \theta}-\frac{\tilde{U}_\theta^{\,2}}{r}+\tilde{U}_z\frac{\partial \tilde{U}_r}{\partial z}+\frac{\partial \tilde{P}}{\partial r}=\frac{1}{Re}\left[\frac{\partial^2 \tilde{U}_r}{\partial r^2}+\frac{1}{r}\frac{\partial \tilde{U}_r}{\partial r}-\frac{\tilde{U}_r}{r^2}+\frac{1}{r^2}\frac{\partial^2 \tilde{U}_r}{\partial \theta^2}-\frac{2}{r^2}\frac{\partial \tilde{U}_\theta}{\partial \theta}+\frac{\partial^2 \tilde{U}_r}{\partial z^2}\right] \tag{2}$$

θ-momentum:

$$\frac{\partial \tilde{U}_\theta}{\partial t}+\tilde{U}_r\frac{\partial \tilde{U}_\theta}{\partial r}+\frac{\tilde{U}_\theta}{r}\frac{\partial \tilde{U}_\theta}{\partial \theta}+\frac{\tilde{U}_r\tilde{U}_\theta}{r}+\tilde{U}_z\frac{\partial \tilde{U}_\theta}{\partial z}+\frac{1}{r}\frac{\partial \tilde{P}}{\partial \theta}=\frac{1}{Re}\left[\frac{\partial^2 \tilde{U}_\theta}{\partial r^2}+\frac{1}{r}\frac{\partial \tilde{U}_\theta}{\partial r}-\frac{\tilde{U}_\theta}{r^2}+\frac{1}{r^2}\frac{\partial^2 \tilde{U}_\theta}{\partial \theta^2}+\frac{2}{r^2}\frac{\partial \tilde{U}_r}{\partial \theta}+\frac{\partial^2 \tilde{U}_\theta}{\partial z^2}\right] \tag{3}$$

z-momentum:

$$\frac{\partial \tilde{U}_z}{\partial t}+\tilde{U}_r\frac{\partial \tilde{U}_z}{\partial r}+\frac{\tilde{U}_\theta}{r}\frac{\partial \tilde{U}_z}{\partial \theta}+\tilde{U}_z\frac{\partial \tilde{U}_z}{\partial z}+\frac{\partial \tilde{P}}{\partial z}=\frac{1}{Re}\left[\frac{\partial^2 \tilde{U}_z}{\partial r^2}+\frac{1}{r}\frac{\partial \tilde{U}_z}{\partial r}+\frac{1}{r^2}\frac{\partial^2 \tilde{U}_z}{\partial \theta^2}+\frac{\partial^2 \tilde{U}_z}{\partial z^2}\right] \tag{4}$$

where $Re\equiv U_{inj}a/\nu$ is the mean flow Reynolds number and U_{inj} is the tangential mean inflow velocity. Furthermore, for a bidirectional motion exhibiting a single mantle, an incompressible, rotational, slightly viscous solution may be used to represent the mean flow. This is given by[2]

$$U_r=-\kappa\frac{1}{r}\sin(\tfrac{1}{2}\pi r^2)\,;\;\; U_\theta=\frac{1-e^{-Vr^2/4}}{r(1-e^{-V/4})}\,;\;\; U_z=2\pi\kappa z\cos(\pi r^2) \tag{5}$$

where

$$\kappa\equiv\frac{Q_i}{2\pi l}=\frac{A_i}{2\pi aL}=\frac{1}{2\pi\sigma l}=\frac{1}{2\sqrt{2}Sl}\,;\;\; V\equiv 2\pi\kappa Re=\frac{Re}{\sigma}\frac{a}{L}=\frac{\bar{Q}_i}{L\nu} \tag{6}$$

Note that V is the vortex Reynolds number and σ is the modified swirl number related to the conventional, unidirectional swirl number via $(\sqrt{2}/\pi)S$.

C. Linear Stability Theory

It must be emphasized that the mean flow described above is one possible solution. Its uniqueness is not demonstrated and its existence is not sufficient to ensure that the solution will be observed in practice. Our analysis investigates its stability. As with most dynamical systems, the mean flow which is continuously excited by the injection process may exhibit two types of responses with respect to this forcing. First, there is the so-called forced response, whose amplitude is of the same order as that of the forcing amplitude. Second, an eigenresponse may be rendered, the amplitude of which can grow significantly larger than the forcing amplitude. The amplitude of the eigenresponse may become unbounded. Such behavior is commensurate with micro events, such as small non-homogeneities in injection, generating a macro phenomenon that translates into appreciable growth in amplitude. The latter is characteristic of intrinsic instabilities. Obviously, determining the physical characteristics of the eigenresponse (including the attendant amplification rate, frequency, spatial dependency, etc.) is essential and constitutes the main goal of this study.

In analyzing the bidirectional vortex, the instantaneous flow may be assumed to be a juxtaposition of the basic flow and the fluctuation whose growth must be determined. This is mathematically achieved by writing:

$$\tilde{M} = M + \hat{m} \tag{7}$$

Here $\tilde{M}$ represents the instantaneous flow, M can be any component of the flowfield (e.g., velocity or pressure), and $\hat{m}$ is a physical quantity that represents possible fluctuations. All fluctuating quantities can be written as:

$$\hat{m} = m(r)\exp\left[i(q\theta + \alpha z - \omega t)\right] \tag{8}$$

where the function $m(r)$ is complex and represents the fluctuating amplitudes (u_r, u_θ, u_z, p), q is real and represents the tangential (i.e., azimuthal) wave number; α and ω are complex quantities (dimensionless) which are suitably subdivided into real and imaginary parts:

$$\alpha = \alpha_r + i\alpha_i, \quad \omega = \omega_r + i\omega_i \tag{9}$$

Note that α_r represents the longitudinal wave number and ω_r is the dimensionless circular frequency. The dimensional frequency is given by $f = \omega_r U_{inj}/(2\pi a)$. The amplification of the amplitude with respect to time and distance z can be assessed from ω_i and $-\alpha_i$, respectively. According to the temporal theory for which $\alpha_i = 0$, fluctuations can only grow in time, and the growth is prescribed by the temporal rate ω_i. Conversely, spatial theory for which $\omega_i = 0$ permits fluctuations to grow only in z, and their local amplification is dependent on the spatial growth rate $-\alpha_i$.

III. Procedure

A. Stability Equations and Boundary Conditions

The Linearized Navier Stokes (LNS) equations can be obtained by substituting the instantaneous variables from Eq. (7) into Eqs. (1)–(4). One could then subtract the basic flow component from the resulting equations and follow by applying the normal mode decomposition of Eq. (8). The outcome is a set of LNS equations of the form:

$$\frac{\mathrm{d}u_r}{\mathrm{d}r} + \frac{u_r}{r} + iq\frac{u_\theta}{r} + i\alpha u_z = 0 \tag{10}$$

$$-i\omega u_r + U_r\frac{\mathrm{d}u_r}{\mathrm{d}r} + u_r\frac{\mathrm{d}U_r}{\mathrm{d}r} + iq\frac{U_\theta}{r}u_r - \frac{2U_\theta u_\theta}{r} + i\alpha U_z u_r + \frac{\mathrm{d}p}{\mathrm{d}r}$$

$$= \frac{1}{Re}\left[\frac{\mathrm{d}^2 u_r}{\mathrm{d}r^2} + \frac{1}{r}\frac{\mathrm{d}u_r}{\mathrm{d}r} - \frac{u_r}{r^2} - \frac{q}{r^2}u_r - \frac{2}{r^2}iqu_\theta - \alpha^2 u_r\right] \tag{11}$$

$$-i\omega u_\theta + U_r \frac{\mathrm{d}u_\theta}{\mathrm{d}\theta} + u_r \frac{\mathrm{d}U_\theta}{\mathrm{d}r} + iq\frac{U_\theta}{r}u_\theta + \frac{U_r u_\theta + U_\theta u_r}{r} + i\alpha U_z u_\theta + \frac{iq}{r}p$$

$$= \frac{1}{Re}\left[\frac{\mathrm{d}^2 u_\theta}{\mathrm{d}r^2} + \frac{1}{r}\frac{\mathrm{d}u_\theta}{\mathrm{d}r} - \frac{u_\theta}{r^2} - \frac{q^2}{r^2}u_\theta + \frac{2}{r^2}iqu_r - \alpha^2 u_\theta\right] \tag{12}$$

$$-i\omega u_z + U_r \frac{\mathrm{d}u_z}{\mathrm{d}z} + u_r \frac{\mathrm{d}U_z}{\mathrm{d}r} + iq\frac{U_\theta}{r}u_z + i\alpha U_z u_z + \frac{\mathrm{d}U_z}{\mathrm{d}z}u_z + i\alpha p = \frac{1}{Re}\left[\frac{\mathrm{d}^2 u_z}{\mathrm{d}r^2} - \frac{1}{r}\frac{\mathrm{d}u_z}{\mathrm{d}r} - \frac{q}{r^2}u_z - \alpha^2 u_z\right] \tag{13}$$

Since disturbances are not permitted along the wall, three boundary conditions may be written for the disturbance amplitudes, namely,

$$u_r = u_\theta = u_z = 0; \;\; r = 1 \tag{14}$$

B. Boundary Conditions at the Centerline

Equations (10)–(13) require six boundary conditions. For closure, three additional boundary conditions are needed, and these can be obtained at $r = 0$. In fact, a special treatment near the axis can be attempted by expanding the LNS equations using Taylor series expansions. To start, however, the basic flowfield must be expanded. At $r = 0$, one gets

$$\begin{cases} U_r = -\kappa\pi r + \frac{1}{6}\kappa\pi^3 r^5 + O(r^6) = -\kappa\pi r + O(r^4) \\ U_\theta = \frac{1}{4}\kappa_0 V r - \frac{1}{32}\kappa_0 V^2 r^3 + O(r^4) \\ U_z = 2\pi\kappa z - \pi^3\kappa z r^3 + O(r^4) \end{cases} \tag{15}$$

where $\kappa_0 = 1/(1-e^{-V/4})$. The perturbation is assumed to be analytical at $r = 0$ so that it may be sought by regular expansion. We use

$$u_r = \sum_{n=0}^{\infty} v_n r^n, \quad u_\theta = \sum_{n=0}^{\infty} w_n r^n, \quad u_z = \sum_{n=0}^{\infty} u_n r^n, \quad p = \sum_{n=0}^{\infty} p_n r^n \tag{16}$$

Likewise, the steady component can be expanded as in

$$U_z = f(z)\sum_{n=0}^{\infty} A_n r^n, \quad U_r = \sum_{n=0}^{\infty} B_n r^n, \quad U_\theta = \sum_{n=0}^{\infty} C_n r^n \tag{17}$$

These expansions are substituted back into Eqs. (10)–(13) and segregated: one is left with three systems, with four equations in each. These are

System 1:
$$\begin{cases} v_0 + iqw_0 = 0 \\ (1+q^2)v_0 + 2iqw_0 = 0 \\ 2iqv_0 - w_0(1+q^2) = 0 \\ -q^2 u_0 = 0 \end{cases} \tag{18}$$

System 2:

$$\begin{cases} 2v_1 + iqw_1 = -i\alpha u_0 \\ -q^2 v_1 - 2iqw_1 = Re\left(iqC_0 v_0 - 2C_0 w_0\right) \\ 2iqv_1 - q^2 w_1 = Re\left[iqp_0 + C_0 p_0 + w_0(iqC_0 + B_0)\right] \\ u_1(1-q^2) = iqReC_0 u_0 \end{cases} \tag{19}$$

System 3 (one-by-one):

$$n \geq 0 \qquad (n+3)v_{(n+2)} + iqw_{(n+2)} + i\alpha u_{(n+1)} = 0 \tag{20}$$

$$\left[(n+2)^2 - (1+q^2)\right]v_{(n+2)} - iReqC_0 v_{(n+1)} - 2iqw_{(n+2)} + 2ReC_0 w_{(n+1)} - Re(n+1)p_{(n+1)}$$

$$= Re\left\{\left(\frac{\alpha^2}{Re} - i\omega\right)v_n + \sum_{j=0}^{n}\left[(i\alpha fA_j + iC_{(i+1)} + (j+1)B_{(j+1)})v_{(n-j)} + (n-j+1)B_j v_{(n-j+1)} - 2C_{(j+1)}w_{(n-j)}\right]\right\} \tag{21}$$

$$2iqv_{(n+2)} - ReC_0 v_{(n+1)} + ((n+2)^2 - (1+q^2))w_{(n+2)} - (iqReC_0 + B_0)w_{(n+1)} - iqRep_{(n+1)}$$

$$= Re\left\{\left(\frac{\alpha^2}{Re} - i\omega\right)w_n + \sum_{j=0}^{n}\left[(B_{(j+1)} + i\alpha fA_j + iqC_{(j+1)})w_{(n-j)} + (n-j+1)w_{(n-j+1)} + ((j+2)C_{(j+1)})v_{(n-j)}\right]\right\} \tag{22}$$

$$\left[(n+2)^2 - q^2\right]u_{(n+2)} - (\alpha^2 - iRe\omega)u_n - i\alpha Rep_n$$

$$= Re\sum_{i=1}^{n}\left\{\left[(f' + i\alpha f)A_j + iqC_{(j+1)}\right]u_{(n+1)} + (n-j+1)u_{(n-j+1)}B_{(j)} + f(j+1)A_{(j+1)}v_{(n-j)}\right\} \tag{23}$$

After some algebra, the boundary conditions for increasing azimuthal wave numbers are found at $r = 0$. These are:

$$\begin{cases} q = 0 \rightarrow u_r(0) = u_\theta(0) = \dfrac{\mathrm{d}u_z}{\mathrm{d}r}(0) = 0 \\ q = 1 \rightarrow \dfrac{\mathrm{d}u_r}{\mathrm{d}r}(0) = \dfrac{\mathrm{d}u_\theta}{\mathrm{d}r}(0) = u_z(0) = 0 \\ q \geq 2 \rightarrow u_r(0) = u_\theta(0) = u_z(0) = 0 \end{cases} \tag{24}$$

Equation (14) can be augmented by Eq. (24) to constitute the needed auxiliary conditions of a well posed differential problem.

C. Spatial Theory

Being homogeneous, Eqs. (10)–(14), and (24) give rise to an eigenvalue problem. As usual, the outcome will be non-trivial only when the problem is singular and, therefore, expressible by an implicit dispersion relation between the key parameters:

$$F(\alpha, \omega, q, z, Re, \kappa) = 0 \tag{25}$$

According to spatial theory, α can be calculated from Eq. (25) by fixing (Re, q, ω) and changing z. The solution is obtained numerically, using a shooting technique that will be further discussed below. This will permit the calculation of perturbed amplitudes such as u_r, u_θ, u_z, and p.

D. Temporal Theory

Physically, each eigenmode represents a nonzero perturbation solution that can satisfy the homogeneous system of equations. The mean flow is considered to be linearly unstable when the local eigenmode, being initialized with a small amplitude, grows with time. By identifying the most amplified eigenmode at a given location, one is able to predict the often undesirable or unsafe frequencies and wavelengths associated with instability. The singularity of the problem inherent in Eq. (25) translates into a set of possible values for ω given fixed values of $(\alpha, q, z, Re, \kappa)$. The full set is called the *spectrum of the mathematical operator*; here, it can be obtained directly by matrix inversion of the resulting differential problem:

$$[\mathbf{A}][\mathbf{Y}] = \omega[\mathbf{B}][\mathbf{Y}] \tag{26}$$

where $[\mathbf{A}]$ and $[\mathbf{B}]$ are differential operators (see Appendix) and $[\mathbf{Y}]$ is the vector $(u_r, u_\theta, u_z, p)^T$. Equation (26) represents the temporal eigenvalue problem and enables us to extract ω directly. Note that it is also possible to solve for ω using an iterative shooting technique.

E. Shooting Method

Unlike the temporal approach in which ω can be rendered directly from the LNS system, it is impossible to isolate α_i when spatial disturbances are manifested at constant ω; the spatial technique requires the use of iterative methods to calculate α.

To set the stage for an efficient iteration routine, it is expedient to rearrange Eqs. (10)–(13) and reduce them to a set of six first-order differential equations. For that purpose, a special treatment following the lines described by Malik[23] can be adopted. Accordingly, $\mathrm{d}u_r/\mathrm{d}r$ is extracted from the continuity equation and substituted into the second order *r*-momentum equation, thus eliminating it from Eq. (11). Forthwith, Eq. (11) is reduced to a first order ODE for the pressure, enabling us to transform the LNS set into

$$\frac{\mathrm{d}Z_i}{\mathrm{d}r} = [\mathbf{C}]\, Z_j, i = 1, 2, \ldots, 6\ ;\ [\mathbf{Z}] = \left\{ u_r, u_\theta, \frac{\mathrm{d}u_\theta}{\mathrm{d}r}, u_z, \frac{\mathrm{d}u_z}{\mathrm{d}r}, p \right\}^T \tag{27}$$

The coefficient matrix $[\mathbf{C}]$ is posted in the Appendix. To admit a non-trivial solution, one of the boundary conditions must be non-homogeneous; this role can be performed by the pressure. One can set

$$u_\theta(1) = u_z(1) = 0 \quad \text{and} \quad p(1) = 1 \ \text{(in lieu of } \mathrm{d}p/\mathrm{d}r = 0\text{)} \tag{28}$$

In this case, the pressure condition acts as a normalization relation. After failing to reach convergence by Newton-Raphson descent, the solution is iterated using Muller's 3-point quadratic approximation (in conjunction with a shooting algorithm) until the boundary condition of the radial amplitude at the wall $u_r(1) = 0$ is secured.

F. Discretization

Discretization of the disturbed system is based on a spectral collocation method.[24] Accordingly, we define $\xi = 2r - 1 \in [-1, 1]$ and choose T_N to be the *N*th-order Chebyshev polynomial. The $N+1$ collocation points are:

$$\xi_i = \cos\left(\frac{\pi i}{N}\right) \qquad i = 0, \ldots, N \tag{29}$$

Equation (29) enables us to calculate the so-called Gauss-Lobatto points. Subsequently, the amplitude function ψ can be interpolated using the polynomial form $\psi(\xi) = \sum \lambda_i \psi(\xi_i)$, where λ_i denotes a Lagrangian multiplier

$$\lambda_i(\xi) = \left(\frac{1 - \xi_i^2}{\xi - \xi_i}\right)(-1)^{i+1} \frac{T_N'}{N^2 c_i} \tag{30}$$

Here T_N' is the derivative of Nth Chebyshev polynomial. The $N+1$ discrete values of $\psi_i = \psi(\xi_i)$ are originally unknown. Their accuracy depends on the size of N. As ψ is a solution of a differential problem, a tacit relation can be obtained between the derivative ψ' and ψ itself. After some algebra, one finds

$$D_{ik} = \frac{c_i}{c_k}\frac{(-1)^{k+i}}{(\xi_i - \xi_k)}; \quad i \neq k \;\; ; \;\; D_{ii} = -\frac{\xi_i}{2(1-\xi_i^2)} \; ; \quad i = 1,...,N-1 ; \;\; D_{00} = -D_{NN} = \frac{2N^2+1}{6} \tag{31}$$

where $c_0 = c_N = 2,\ c_i = 1,\ i = 1,...,N-1$ and the discretized equations can be written as

$$\frac{\mathrm{d}\psi}{\mathrm{d}\xi}(\xi_i) = \sum_{k=0}^{N} D_{ik}\psi_k \tag{32}$$

where ψ represents the amplitude components, namely, $\psi = (u_r, u_\theta, u_z, p)$.

IV. Results and Discussion

The two theories discussed earlier are tested for Culick's profile before being applied to the bidirectional vortex. As mentioned earlier, with the temporal approach, α_i can be set to zero, q, κ and Re held constant, and ω can be calculated from the dispersion relation defined by Eq. (25) and giving rise to Eq. (26). Conversely, per spatial theory, ω_i can be set to zero before repeating the same procedure. The advantage of the temporal theory lies in its ability to predict the full spectrum at fixed spatial location. In contrast, the solution proceeding from spatial theory must rely on guesswork, shooting, and trial before convergence can be achieved. In either case, the most essential eigenvalue is the most unstable one.

A. Verification and Grid Refinement

To check the robustness of our code, we have carried out a point-by-point verification by comparing our results to data published using the known Taylor/Culick profile.[14] Table 1 illustrates the agreement between our predictions and published results (specifically, those given in Table III of Griffond, Casalis and Pineau[14]).

In Table 2 we compare results from both temporal and spatial theories; a perfectly congruent agreement may be seen to exist as the two theories converge to nearly identical numerical values. The difference is that, in the left column, ω is determined at fixed α, whereas the opposite is true in the right column where the spatial theory is used. In ensuring proper grid refinement, the number of discretization points is first set at $N = 100$. This number counts the collocation points in the Chebyshev polynomial used to approximate the derivatives in Eq. (32). As this number is repeatedly doubled, results continue to shift appreciably until a value of $N \simeq 600$ is reached. At this point, a well defined trend emerges, namely, one that is no longer susceptible to change with increasing N.

As shown in Fig. 2, the scatters for N = 500 and 600 become almost indiscernible. Convergence, which is harder to achieve at q = 1, is reached near a value that is nearly four times larger than that attributed to the analogous Taylor/Culick profile where $N \simeq 150$ is usually used. In the same vein, it may be noted that the spatial procedure is about three times faster converging than the temporal counterpart. In Table 2, for example, as α is calculated at constant ω (to render the right-hand-side column), convergence is visible as early as N = 200.

Table 1. Eigenvalues of the Culick profile at ω = 90, z = 10, q = 0, and Re = 4,500

	Griffond, Casalis and Pineau[14]		Current code	
Mode	α_r	α_i	α_r	α_i
1	6.0952945656	–1.0787998140	6.0952945724	–1.0787998101
2	3.3264285366	–0.1095525589	3.3264285380	–0.1095525581
3	2.6013223310	0.1322870315	2.6013223554	0.1322830025

Table 2. Prediction for the vortex chamber at z = 10, q = 0, and Re = 5,000

q		Temporal theory	Spatial theory
0	α	$3 - 0.3i$	$3.0013272433 - 0.3001703496i$
	ω	$1.1447302811 - 0.1810676630i$	$1.1447302811 - 0.1810676630i$
1	α	$3 - 0.3i$	$2.9895942062 - 0.301893219i$
	ω	$0.0345603998 - 0.0232676414i$	$0.0345603998 - 0.0232676414i$
2	α	$3 - 0.3i$	$3.0013524374 - 0.3001858499i$
	ω	$1.11653081200 - 0.0613034759i$	$1.11653081200 - 0.0613034759i$

B. Spatial Trends

According to available experimental results, it has been often submitted that the spatial theory stands to provide the better option in studying instability in rocket motors. For this reason, we adopt it here as our primary method. The temporal theory is also very useful; for example, it can expedite the evaluation of initial guesses needed to perform the spatial analysis. To begin, we recall that α is the complex number from which the wave number α_r and amplification rate $-\alpha_i$ can be obtained. Also, $\omega_r/(2\pi)$ represents the circular frequency of the unsteady perturbation. In what follows, we examine the effect of Re and κ (which combines the swirl number and aspect ratio) for different tangential modes q. To cover a broad range of operating parameters, we take $Re \in [10^4 - 10^6]$, $\kappa \in [10^{-4} - 10^{-1}]$, and calculate the vortex Reynolds number from $V = 2\pi\kappa Re$.[2]

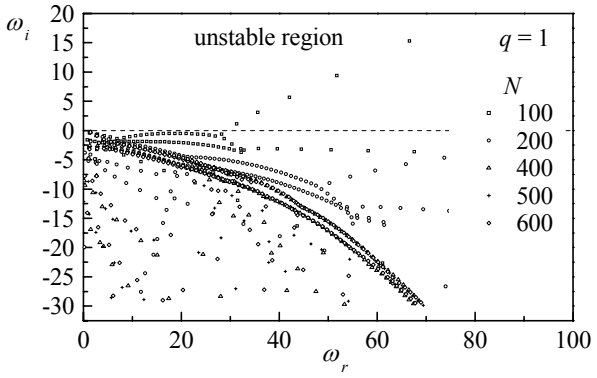

Figure 2. Mesh refinement at the first tangential mode showing asymptotic convergence near N = 600. Based on temporal theory we use α = 3, z = 1.5, Re = 10,000 and κ = 0.1. Everywhere else, we take q = 0 unless stated otherwise.

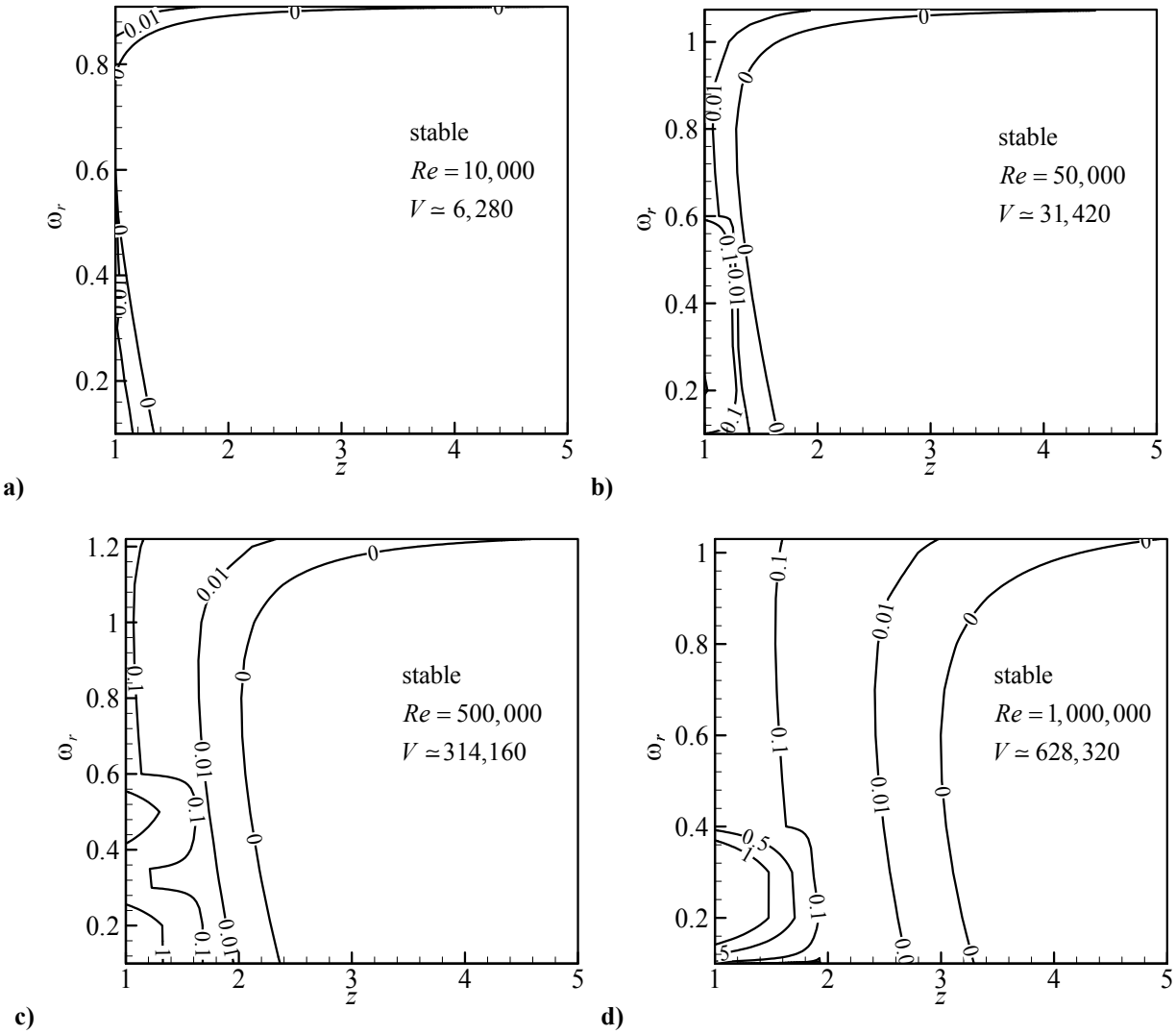

Figure 3. Iso-n factors for κ = 0.1. Here $\omega_i = 0$ and $\omega_r = \omega = 2\pi af/U_{inj}$. Note that n does not exceed unity.

The first series of plots illustrates the effect of increasing the Reynolds number at a fixed value of κ. To capture this behavior effectively, the iso-n curves (which represent the exponential spatial amplification rates) are produced in Fig. 3 at four different values of Re spanning two orders of magnitude. This is done at fixed $\kappa = 0.1$ and a range of axial locations ranging between 1 and 5. No value above 5 is chosen for z because of the application in question being limited to rather short chambers.[6,7]

In relation to n, the amplitude of the wave can be obtained by integrating the local amplification using:

$$A(z,\omega) = A_0 e^n \quad ; \quad n(z,\omega) = \int_{z_0(\omega)}^{z} -\alpha_i(\xi,\omega)\,\mathrm{d}\xi \tag{33}$$

Here $z_0(\omega)$ denotes the first axial position where marginal stability is reached; as such, A_0 represents the marginally stable amplitude along the neutral curve where n vanishes.

Some useful features can be inferred from Fig. 3. For example, the motor appears to be most unstable near the headend and most stable further downstream, near the hypothetical swirl injection plane. As the Reynolds number is increased, the region of instability is broadened to the extent that, at the relatively high value of $Re = 10^6$, no stable portion appears to exist under $z = 3$. However, this may be a spurious effect considering that the unstable regions remain characterized by unusually small rates of amplification. In fact, n remains so small that the flow in the unstable region is unlikely to breakdown; the latter is projected to occur past $n \simeq 7$ in model solid rocket motors; it is remarkable that this value is never reached by n in this study. A two-dimensional stability analysis in which radial and streamwise coupling is fully integrated may be needed to capture the attendant behavior because of the characteristic size of the bidirectional vortex chamber. A nonlinear stability analysis may also help in elucidating the possible coupling between tangential modes. Along similar lines, the relatively large amplification observed near the headend may be justified by the absence of viscosity in our model near the endwall region. A higher-order flow profile may be needed to capture the Ekman-type boundary layers that are expected to form at the headend. In the absence of more refined model, the current predictions may remain inconclusive in that locality.

In a companion paper by the authors,[25] the stability attributes of solid and hybrid rockets with headend injection are closely examined. It may be interesting to note that the trends depicted in Fig. 3 are nearly reversed when contrasted with those of solid and hybrid rockets. More on this will soon follow. For now, it may suffice to say that, instead of observing an unbounded region of stability, the bidirectional vortex exhibits a well delineated stability domain. Instead of seeing a frequency below which the flow is unconditionally stable, the horizontal segments of the neutral curves in Fig. 3 signal the presence of a limiting frequency above which the flow may become unstable. Above that frequency, however, it is not possible to calculate the iso-*n* factors needed to estimate the amplification rate. The limiting frequency corresponds to the upper branch of each neutral curve that gradually asymptotes to a constant value with increasing z. These neutral curves are compared in Fig. 4 at four select Reynolds numbers.

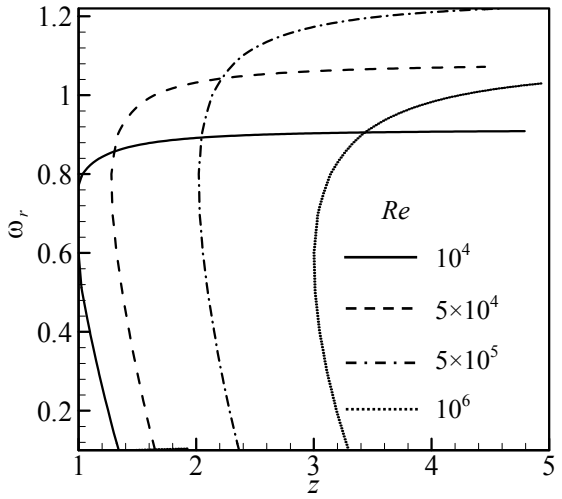

Figure 4. Neutral curves for $\kappa = 0.1$ and four different values of the Reynolds number.

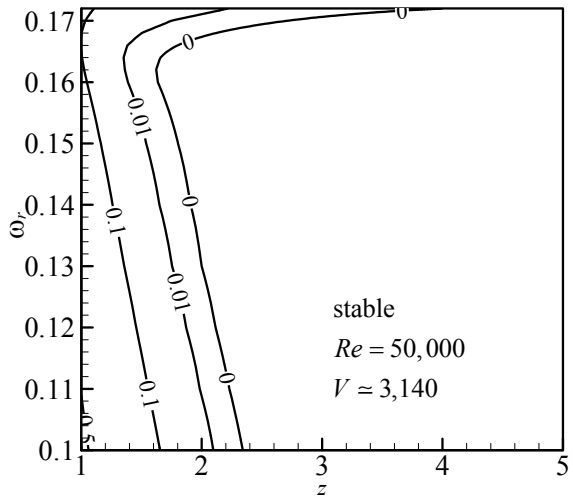

Figure 5. Iso-*n* factors for $\kappa = 0.01$.

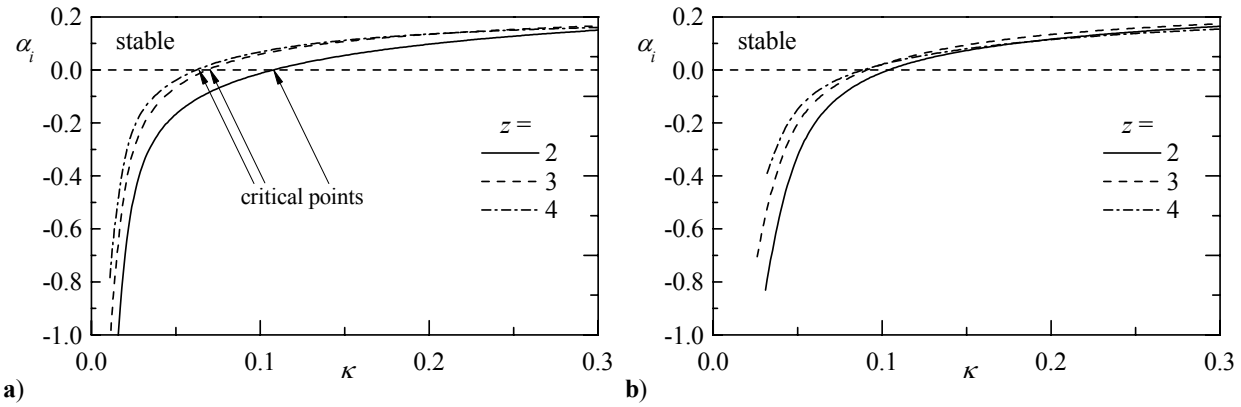

Figure 6. Effect of varying the inflow parameter κ on stability. This is shown at three equally spaced axial positions, a fixed radial position of r = 0.5, and two dimensionless frequencies: a) ω_r = 0.5 and b) ω_r = 1.

Note that the asymptotic frequencies delineating the stable domain vary with the Reynolds number. They increase with Re, reach a maximum around $Re = 5\times10^5$, then decrease again. In contrast to the asymptotic frequency, the stability domain continues to shift downstream as Re is increased. It may be useful to note that more than one mode can be found at a certain frequency and location; however, our main concern has been on identifying the most unstable case. Each point on the curves of the aforementioned figures is hence generated for the most amplified mode associated with a given frequency and axial location.

The influence of κ is briefly illustrated (for one case) in Fig. 5 where it is reduced by one order of magnitude relative to Fig. 4. Being the ratio of the injector cross-sectional area to the surface-area of the chamber, a reduction in this parameter at constant flowrate is equivalent to increasing the swirl velocity. We recall that κ is inversely proportional to the modified swirl number and chamber aspect ratio. As shown on the graph, increasing swirl reduces the range of stable frequencies by one order of magnitude. Surprisingly, this reduction in stable frequencies is not accompanied by an increase in the *n*-factor. The latter remains confined to such small amplification rates that they cannot be a cause for concern. We also realize that the reduction in stable frequencies is only an artifact. Since $f = \omega_r U_{inj}/(2\pi a)$, the actual stable frequencies depend on the product of ω_r and U_{inj}. So while reducing κ will decrease the range of stable ω_r, it will proportionally increase the swirl injection velocity U_{inj} to the extent of offsetting the compression of the dimensionless range. We thus deduce that, according to the present model, increasing swirl will be of little consequence on the amplification rate and may actually serve as a stabilizing agent.

In Fig. 6, we attempt to characterize the effect of swirl on the spatial growth rate α_i at several axial stations and increasing frequency. First, we observe an upward movement in the stability curves as we approach the downstream end of the chamber. This confirms our earlier conclusion regarding the flow being the least stable near the headwall. Second, we note that as κ is decreased, an increase in the spatial growth rate is observed. This also supports the apparent effect of swirl on reducing the dimensionless range for stability. Third, the critical values of κ are found to be smaller at increasing distance from the headwall but larger as we double the dimensionless frequency (Fig. 6b). At the outset, increasing the frequency is seen to have a destabilizing role, unlike the spatial increase in z.

At $Re = 5\times10^5$ and $z = 2$, the most excited frequency of the bidirectional vortex is seen to occur at a frequency of 2.775 (see Fig. 7). Based on Fig. 4, the flow at this Reynolds number is unstable. The sudden bump in the pressure corresponds to the most hazardous frequency from the standpoint of design. Aside from this peak, we have been unable to determine any other undesirable frequencies in the unstable regions, especially, while screening for $z \le 1.5$. Thus, even in the unstable region near the headwall, no sudden jumps

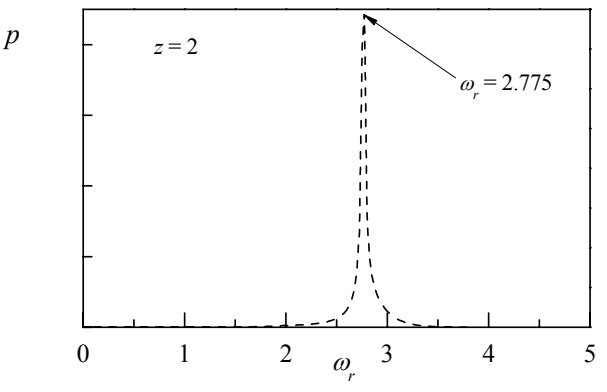

Figure 7. Spiking pressure amplitude at the most amplified or unsafe frequency. This is shown for κ = 0.1, r = 0.5, z = 2, and Re = 500,000.

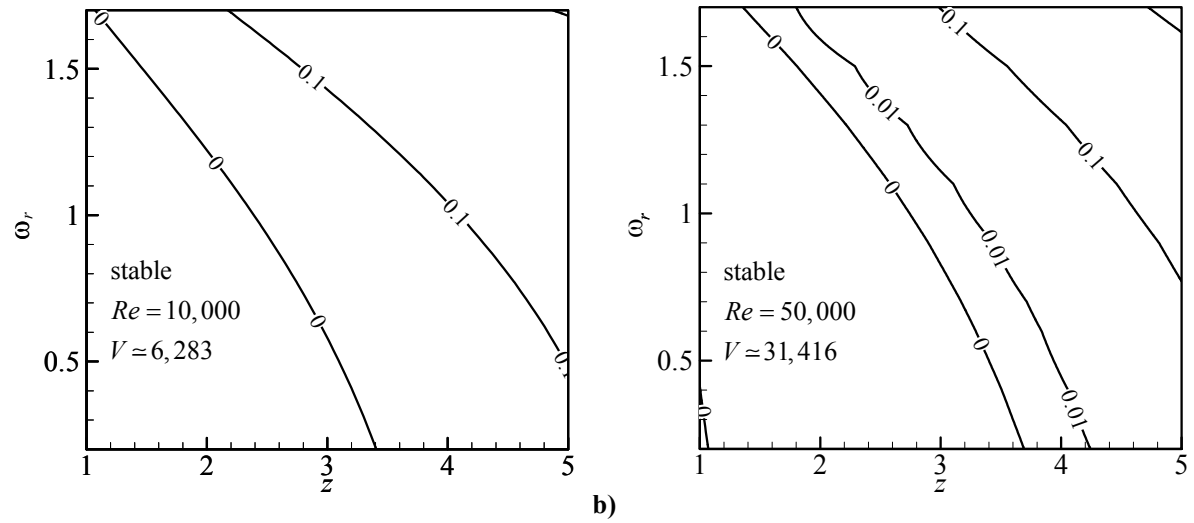

Figure 8. Iso-*n* factors for q = 1 and κ = 0.1.

in pressure or velocity fluctuations could be observed. No undesirable frequencies could be detected at any other location for this mode.

Having covered some of the features of the flow under the auspices of $q = 0$, we now shift our focus to the first tangential mode, $q = 1$; this is characterized in Fig. 8 at two increasing Reynolds numbers and a constant inflow parameter. This is the second most likely mode to be present as it requires less energy to excite than other, higher order tangential counterparts. A sharp contrast can be effectively drawn by comparing Figs. 8a,b to Figs. 3a,b at two increasing Reynolds numbers. An interesting behavior may be seen to accompany this case considering that the region of stability shifts to the opposite chamber end relative to the zeroth mode. Now the stability domain is anchored at the headend and becomes progressively more unstable as we move downstream toward to the virtual injection plane. This may be attributed to the alternating waveform that accompanies the first tangential mode. As

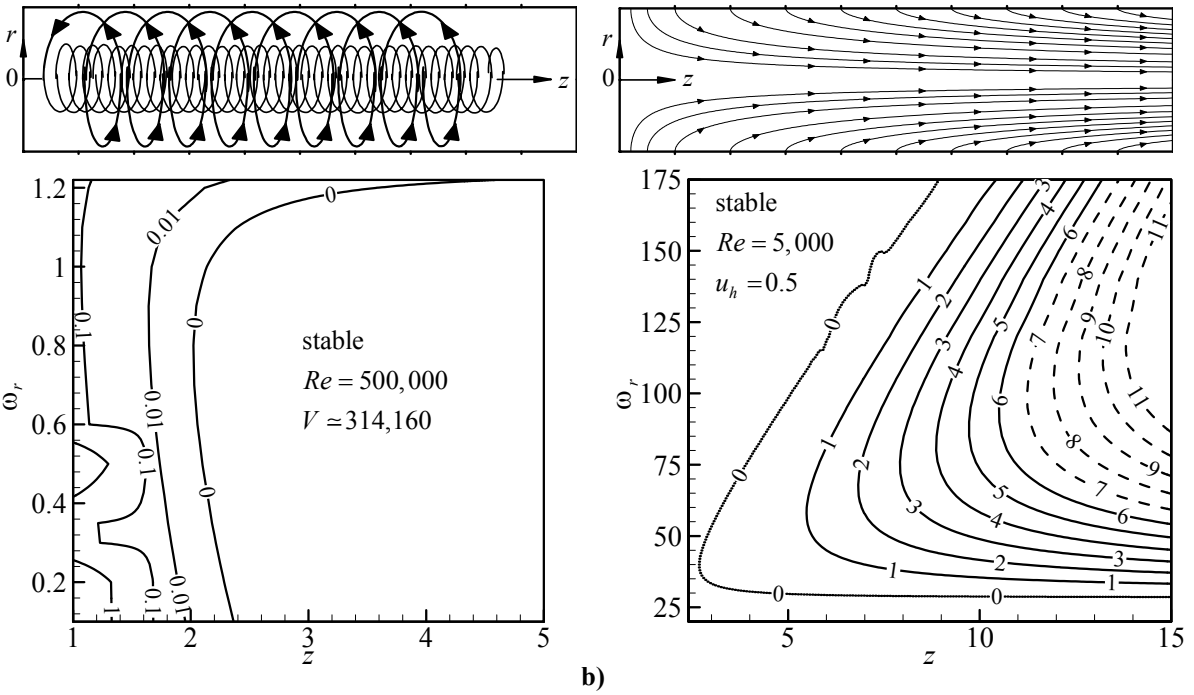

Figure 9 Contrast between iso-*n* graphs and their corresponding stability trends obtained for a) the bidirectional vortex (*Re* = 500,000) and b) the Majdalani-Vyas profile for solid rocket motors with headend injection (*Re* = 5,000 and u_h = 0.5).

the tangential mode number is increased, we also note a slight increase in the amplification rate; here too, it remains too small to be a cause for concern. Thus, despite the higher values of n, there is no evidence of excitation energy that can possess the levels needed to trigger flow breakdown.

To further illustrate the unconventional stability response of the bidirectional vortex, a comparison with the classic flow instability solution for the solid rocket motor with headwall injection is presented in Fig. 9. As explained in the companion paper by the authors,[25] the solution in Fig. 9b is also characteristic of the flow instability affecting hybrid rocket engines with large headwall injection. Due to the disparity in physical settings we choose typical operating parameters in each. In both cases, the zeroth tangential instability mode is considered. The first observation concerns the regions of instability which appear to be reversed in the bidirectional vortex. For example, Fig. 9a displays the growing amplification rates up to the breakdown region (shown using broken lines past $n = 6$). Conversely, the n-factor does not exceed unity as we approach the headwall in Fig. 9a. This imparts an unusual stability trait to the bidirectional vortex. The second observation concerns the location and size of the stable domain. While the stable region for the solid rocket motor is manifested to the left (near $z = 0$), it appears to the right in the bidirectional vortex (near $z = L/a$); in both cases, these stations coincide with the main endwall injection plane. Note that the bounded regions shown in Figs. 9a and 9b correspond to the stable and unstable regions, respectively. Furthermore, the unstable region seems to be very narrow in the bidirectional vortex while sustaining very small amplification rates, especially when compared to their counterparts in the solid rocket motor. This represents a highly desirable feature of the flow. Finally, the asymptotic lines delineating minimum and maximum frequencies are in reverse order in both chambers. For example, above a frequency of 28, the classic motor starts to show signs of instability. Thus, while the SRM is susceptible to low frequency instability, the bidirectional vortex appears to be resilient to those. Note that in Fig. 9a, values of ω_r are obtained using a large normalizing factor. The corresponding dimensional frequencies are quite high.

C. Temporal Trends

Results obtained from the temporal theory are summarized in Figs. 10 and 11 where the solution of the

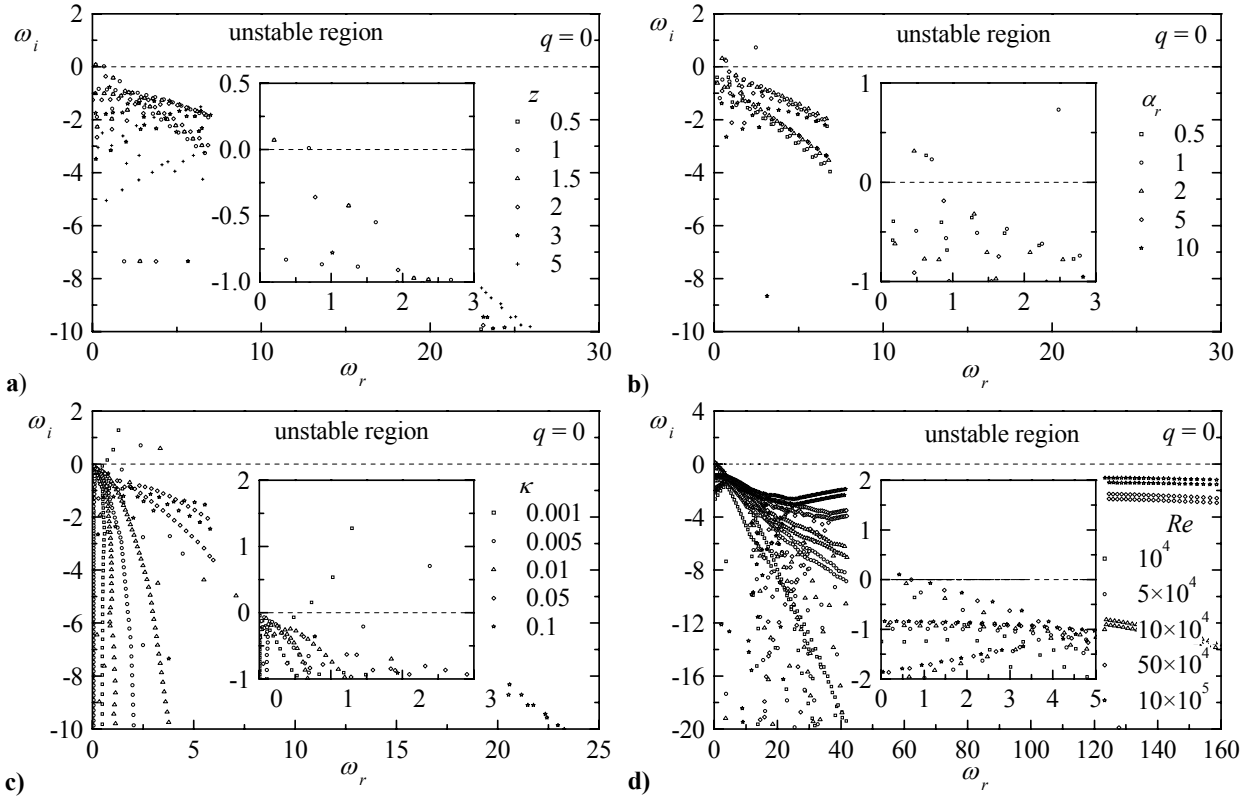

Figure 10. Temporal response at $q = 0$ showing the full spectrum at varying a) z and $\kappa = 0.1$, $\alpha = 3$, and $Re = 100{,}000$; b) α and $\kappa = 0.1$, $z = 0.5$, and $Re = 100{,}000$; c) κ and $z = 2$, $\alpha = 3$, and $Re = 100{,}000$; and d) Re and $\kappa = 0.1$, $z = 2$, and $\alpha = 3$.

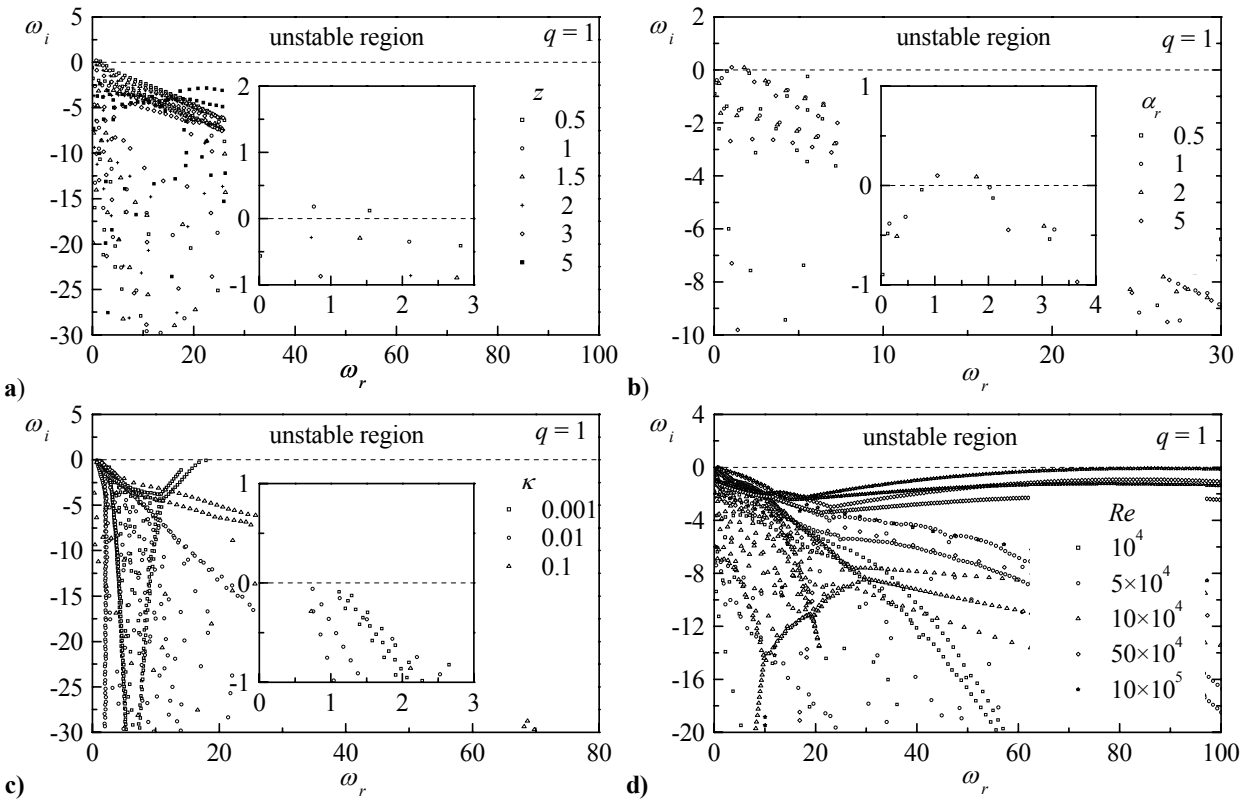

Figure 11. Temporal response at q = 1 showing the full spectrum at varying a) z and κ = 0.1, α = 3, and Re = 100,000; b) α and κ = 0.1, z = 0.5, and Re = 100,000; c) κ and z = 2, α = 3, and Re = 100,000; and d) Re and κ = 0.1, z = 2, and α = 3.

dispersion relation is illustrated for the first two tangential wave numbers, $q = 0,1$. These graphs cover the full spectrum of eigenvalues for different z, wave number α, inflow parameter κ, and Reynolds number Re. Overall, the temporal results confirm the trends projected by the spatial analysis.

For example, Fig. 10a gives the spectrum at different locations in the chamber. By fixing the other three variables (Re, κ, α), a clearer understanding of the flow evolution with z is possible. Upon close examination, it can be seen that the disturbance waves are prone to amplification near the headend, particularly, at very low dimensionless frequencies. This behavior is made more apparent by the magnification shown in the corresponding inset. At higher frequencies, no amplification can be detected.

Next, the effect of the wave number $\alpha = \alpha_r$ is examined in Fig. 10b. Here too, the unstable points are clustered in the low frequency range. The effect of reducing the inflow parameter κ is also seen, in Fig. 10c, to trigger a few unstable points at low frequency. In Fig. 10d, a similar trend is seen to follow from increasing the Reynolds number, although all observed frequencies remain damped for the majority of Reynolds numbers shown, only one unstable point emerges when reaching a value of $Re = 10^6$. In all cases, no amplification can be seen at dimensionless frequencies roughly exceeding a value of 3. Figure 11 reproduces the test cases of Fig. 10 at $q = 1$. Overall, similar trends are depicted except for Fig. 11c where the inflow parameter is varied. As the tangential mode is increased to 1, no amplified frequency can be detected at any κ. This reaffirms $q = 0$ as being the most vulnerable tangential mode. Here too, the amplification rate does not appear to change in any noticeable manner as we move from one wave number to another.

V. Conclusions

In this work, both temporal and spatial stability approaches are tailored to and tested on the bidirectional vortex. At first glance, the spatial theory, appearing to be the most relevant and revealing, has enabled us, at the cost of added numerical complexity, to identify key stability features. These include the destabilizing effects of increasing the swirl number, chamber aspect ratio, and injection Reynolds number. Reducing the inflow parameter, for example, decreases the range of unconditionally stable frequencies (but not necessarily the dimensional ones due to

the inevitable increase in injection velocity); this can be accomplished by either raising the swirl number or further elongating the chamber. We also realize that the endwalls bracketing the forward and aft regions represent critical stability sites as they appear to be the most susceptible to wave amplification at the zeroth and first tangential modes, respectively. Unsurprisingly, the zeroth tangential mode is confirmed to be the most unstable. By comparison to the neutral curves obtained in the analysis of solid and hybrid rockets,[25] the trends here are nearly reversed. The neutral curves of the bidirectional vortex are bounded by an upper branch that asymptotes to a limiting frequency. Above this frequency, the flow becomes unstable, although no evidence of appreciable amplification may be gathered. The iso-*n* factor, which prescribes the amplification rate and transition propensity, remains extremely small, namely, less than unity. This result is reassuring and suggests that the bidirectional motion may be intransigent to wave amplification as swirl may attenuate potentially unstable disturbances by preventing them from growing past tolerable levels. Thus, even in the unstable regions projected by linear theory, wave growth is mitigated to the extent that coherent motion is always retained. Unlike the extended Taylor-Culick profile[22] which is susceptible to resonance at relatively low frequencies,[25] the bidirectional vortex is prone to instability at unusually high frequencies, specifically, at levels that require enormous excitation energy. Thus, unlike classic solid and hybrid flowfields in which resonance can be accentuated by a variety of injection related factors, swirl appears to act as a stabilizing agent. A look at absolute instability and a nonlinear analysis may be warranted to further explore this unusual and highly desirable feature of the bidirectional vortex. In what concerns the model itself, we recognize one limitation of the mean flow profile that lies in its incapacity to account for viscous damping along the chamber walls. The profile used here is incompressible and can only capture the viscous boundary layer connected with the forced vortex forming along the chamber axis. A higher order model may have to be constructed in the hope of producing a more coherent framework. What is needed is a flowfield approximation that can incorporate the boundary layers along both endwall and sidewall. To further enhance the model's prognostic capabilities, inclusion of compressibility effects may be needed because of the large swirl velocities associated with this motion; in fact, large velocities have been repeatedly reported in recent theoretical and experimental investigations. The absence of viscous damping near the headend may be a spurious artifact and one of the reasons for obtaining large amplification rates in that vicinity. What is most interesting is, perhaps, the finding that the bidirectional vortex is unsusceptible to amplification rates that are large enough to trigger breakdown.

Appendix A

Differential operators for Eq. (26):

$$[\mathbf{A}]=\begin{pmatrix}[\mathbf{A_{11}}] & [\mathbf{A_{12}}] & [\mathbf{A_{13}}] & [\mathbf{A_{14}}]\\ [\mathbf{A_{21}}] & [\mathbf{A_{22}}] & [\mathbf{A_{23}}] & [\mathbf{A_{24}}]\\ [\mathbf{A_{31}}] & [\mathbf{A_{32}}] & [\mathbf{A_{33}}] & [\mathbf{A_{34}}]\\ [\mathbf{A_{41}}] & [\mathbf{A_{42}}] & [\mathbf{A_{43}}] & [\mathbf{A_{44}}]\end{pmatrix};\quad [\mathbf{A_{11}}]=\left[\mathbf{D_{ij}}\right]+\frac{1}{\xi_{ij}}[\mathbf{I}],\ [\mathbf{A_{12}}]=\frac{iq}{r}[\mathbf{I}],\ [\mathbf{A_{13}}]=i\alpha[\mathbf{I}],\ [\mathbf{A_{14}}]=[\mathbf{0}] \tag{A1}$$

and $$[\mathbf{A_{21}}]=\left[U_r-\frac{1}{Re}\left(\frac{1}{\xi_{ij}}+\left[\mathbf{D_{ij}}\right]\right)\right]\left[\mathbf{D_{ij}}\right]+\left\{\frac{\mathrm{d}U_r}{\mathrm{d}r}+\frac{1}{\xi_{ij}}\left[iqU_\theta+1+i\alpha U_z+\frac{1}{Re}\left(\left(\frac{1+q}{\xi_{ij}}\right)+\frac{1}{\alpha^2}\right)\right]+i\alpha U_z\right\}[\mathbf{I}] \tag{A2}$$

$$[\mathbf{A_{22}}]=\frac{2}{\xi_{ij}}\left(\frac{iq}{Re}-U_\theta\right)[\mathbf{I}],\ [\mathbf{A_{23}}]=[\mathbf{0}],\ [\mathbf{A_{24}}]=\left[\mathbf{D_{ij}}\right],[\mathbf{A_{31}}]=\left[\left(\frac{\mathrm{d}}{\mathrm{d}r}+\frac{1}{\xi_{ij}}\right)U_\theta-\frac{1}{Re}\frac{2iq}{\xi^2{}_{ij}}\right][\mathbf{I}] \tag{A3}$$

$$[\mathbf{A_{32}}]=\left[U_r-\frac{1}{Re}\left(\left[\mathbf{D_{ij}}\right]-\frac{1}{\xi_{ij}}\right)\right]\left[\mathbf{D_{ij}}\right]+\left\{\frac{1}{\xi_{ij}}\left[iqU_\theta+U_r+\frac{1}{Re}\left(\frac{1+q^2}{\xi_{ij}}\right)\right]+\alpha\left(\alpha+iU_z\right)\right\}[\mathbf{I}] \tag{A4}$$

$$[\mathbf{A_{33}}]=[\mathbf{0}],\ [\mathbf{A_{34}}]=\frac{iq}{\xi_{ij}}[\mathbf{I}],[\mathbf{A_{41}}]=\frac{\mathrm{d}U_z}{\mathrm{d}r}[\mathbf{I}],\ [\mathbf{A_{42}}]=[\mathbf{0}] \tag{A5}$$

$$\left[\mathbf{A_{43}}\right]=\left[U_r-\frac{1}{Re}\left(\left[\mathbf{D_{ij}}\right]-\frac{1}{\xi_{ij}}\right)\right]\left[\mathbf{D_{ij}}\right]+\left[\frac{iqU_\theta}{\xi_{ij}}+\left(\frac{\mathrm{d}}{\mathrm{d}z}+i\alpha\right)U_z+\frac{1}{Re}\left(\frac{q^2}{\xi^2{}_{ij}}+\alpha^2\right)\right]\left[\mathbf{I}\right],\ \left[\mathbf{A_{44}}\right]=i\alpha\left[\mathbf{I}\right] \tag{A6}$$

and
$$\left[\mathbf{B}\right]=\begin{pmatrix}\left[\mathbf{B_{11}}\right] & \left[\mathbf{B_{12}}\right] & \left[\mathbf{B_{13}}\right] & \left[\mathbf{B_{14}}\right]\\ \left[\mathbf{B_{21}}\right] & \left[\mathbf{B_{22}}\right] & \left[\mathbf{B_{23}}\right] & \left[\mathbf{B_{24}}\right]\\ \left[\mathbf{B_{31}}\right] & \left[\mathbf{B_{32}}\right] & \left[\mathbf{B_{33}}\right] & \left[\mathbf{B_{34}}\right]\\ \left[\mathbf{B_{41}}\right] & \left[\mathbf{B_{42}}\right] & \left[\mathbf{B_{43}}\right] & \left[\mathbf{B_{44}}\right]\end{pmatrix};\ \begin{cases}\left[\mathbf{B_{11}}\right]=\left[\mathbf{B_{12}}\right]=\left[\mathbf{B_{13}}\right]=\left[\mathbf{B_{14}}\right]=\left[\mathbf{0}\right]\\ \left[\mathbf{B_{21}}\right]=i\left[\mathbf{I}\right],\ \left[\mathbf{B_{22}}\right]=\left[\mathbf{B_{23}}\right]=\left[\mathbf{B_{24}}\right]=\left[\mathbf{0}\right]\\ \left[\mathbf{B_{31}}\right]=\left[\mathbf{0}\right],\ \left[\mathbf{B_{32}}\right]=i\left[\mathbf{I}\right],\ \left[\mathbf{B_{33}}\right]=\left[\mathbf{B_{34}}\right]=\left[\mathbf{0}\right]\\ \left[\mathbf{B_{41}}\right]=\left[\mathbf{B_{42}}\right]=\left[\mathbf{0}\right],\ \left[\mathbf{B_{43}}\right]=i\left[\mathbf{I}\right],\ \left[\mathbf{B_{44}}\right]=\left[\mathbf{0}\right]\end{cases} \tag{A7}$$

$$\left[\mathbf{D_{ij}}\right]=\begin{pmatrix}D_{11} & D_{12} & \cdots & D_{1N}\\ D_{21} & \mathrm{D}_{22} & \cdots & D_{2N}\\ \vdots & \vdots & \ddots & \vdots\\ D_{N1} & D_{N2} & \cdots & D_{NN}\end{pmatrix},\ \left[\mathbf{I}\right]=\begin{pmatrix}1 & 0 & \cdots & 0\\ 0 & 1 & \cdots & 0\\ \vdots & \vdots & \ddots & \vdots\\ 0 & 0 & \cdots & 1\end{pmatrix},\ \left[\mathbf{0}\right]=\begin{pmatrix}0 & 0 & \cdots & 0\\ 0 & 0 & \cdots & 0\\ \vdots & \vdots & \ddots & \vdots\\ 0 & 0 & \cdots & 0\end{pmatrix} \tag{A8}$$

The coefficient matrix corresponding to the reduced order LNS is given by:

$$[\mathbf{C}]=\begin{pmatrix}C_{11} & C_{12} & 0 & C_{14} & 0 & 0\\ 0 & C_{21} & 0 & 0 & 0 & 0\\ C_{31} & C_{32} & C_{33} & 0 & 0 & 0\\ 0 & 0 & 0 & C_{45} & 0 & 0\\ C_{51} & 0 & 0 & C_{54} & C_{55} & C_{56}\\ C_{61} & C_{62} & C_{63} & C_{64} & C_{65} & 0\end{pmatrix};\ \begin{cases}C_{11}=-\dfrac{1}{r}\ ,\ C_{12}=-\dfrac{iq}{r}\ ,\ C_{14}=-i\alpha,\ C_{21}=1\\ C_{31}=Re\left(\dfrac{U_\theta}{r}+U'_\theta\right)-\dfrac{2iq}{r^2}\\ C_{32}=Re\left(-i\omega+\dfrac{iq}{r}U_\theta+\dfrac{U_r}{r}+i\alpha U_z\right)+\dfrac{1}{r^2}\left(q^2+1\right)+\alpha^2\\ C_{33}=ReU_r-\dfrac{1}{r}\ ,\ C_{36}=Re\dfrac{iq}{r}\end{cases} \tag{A9}$$

and
$$\begin{cases}C_{31}=Re\left(\dfrac{U_\theta}{r}+U'_\theta\right)-\dfrac{2iq}{r^2},\ C_{32}=Re\left(-i\omega+\dfrac{iq}{r}U_\theta+\dfrac{U_r}{r}+i\alpha U_z\right)+\dfrac{1}{r^2}\left(q^2+1\right)+\alpha^2\\ C_{33}=ReU_r-\dfrac{1}{r},\ C_{36}=Re\dfrac{iq}{r},\ C_{45}=1,\ C_{55}=ReU_r-\dfrac{1}{r},\ C_{56}=Re\dfrac{iq}{r}\\ C_{51}=ReU'_z,\ C_{54}=Re\left(-i\omega+\dfrac{iq}{r}U_\theta+i\alpha U_z+\dfrac{\partial U_z}{\partial z}\right)+\dfrac{q^2}{r^2}+\alpha^2,\ C_{64}=i\alpha U_r,\ C_{65}=\dfrac{1}{Re}\left(-i\alpha\right)\\ C_{61}=\dfrac{1}{Re}\left(-\dfrac{q^2}{r^2}-\alpha^2\right)+i\omega+\dfrac{U_r}{r}-U'_r-\dfrac{iq}{r}U_\theta-i\alpha U_z,\ C_{62}=\dfrac{1}{Re}\left(-\dfrac{iq}{r^2}\right)+U_r\dfrac{iq}{r}+2\dfrac{U_\theta}{r},\ C_{63}=\dfrac{1}{Re}\left(-\dfrac{iq}{r}\right)\end{cases} \tag{A10}$$

Acknowledgments

This project is sponsored, in part, by the Faculty CAREER Program of the National Science Foundation, Grant No. CMS-0353518, Program Manager, Dr. Masayoshi Tomizuka. We are deeply grateful for the additional support received through Orbital Technologies Corporation, Madison, WI. We are especially indebted to Dr. Martin J. Chiaverini for his insightful comments and suggestions during the course of this investigation.

References

[1]Vyas, A. B., Majdalani, J., and Chiaverini, M. J., "The Bidirectional Vortex. Part 1: An Exact Inviscid Solution," AIAA Paper 2003-5052, July 2003.

[2]Vyas, A. B., Majdalani, J., and Chiaverini, M. J., "The Bidirectional Vortex. Part 2: Viscous Core Corrections," AIAA Paper 2003-5053, July 2003.

[3]Vyas, A. B., Majdalani, J., and Chiaverini, M. J., "The Bidirectional Vortex. Part 3: Multiple Solutions," AIAA Paper 2003-5054, July 2003.

[4]Fang, D., Majdalani, J., and Chiaverini, M. J., "Simulation of the Cold-Wall Swirl Driven Combustion Chamber," AIAA Paper 2003-5055, July 2003.
[5]Fang, D., Majdalani, J., and Chiaverini, M. J., "Hot Flow Model of the Vortex Cold Wall Liquid Rocket," AIAA Paper 2004-3676, July 2004.
[6]Chiaverini, M. J., Malecki, M. J., Sauer, J. A., and Knuth, W. H., "Vortex Combustion Chamber Development for Future Liquid Rocket Engine Applications," AIAA Paper 2002-2149, July 2002.
[7]Chiaverini, M. J., Malecki, M. J., Sauer, J. A., Knuth, W. H., and Majdalani, J., "Vortex Thrust Chamber Testing and Analysis for O2-H2 Propulsion Applications," AIAA Paper 2003-4473, July 2003.
[8]Chiaverini, M. J., Malecki, M. M., Sauer, J. A., Knuth, W. H., and Hall, C. D., "Testing and Evaluation of Vortex Combustion Chamber for Liquid Rocket Engines," JANNAF 2002.
[9]Knuth, W. H., Bemowski, P. A., Gramer, D. J., Majdalani, J., and Rothbauer, W. J., "Gas-Fed, Vortex Injection Hybrid Rocket Engine," NASA Marshall Space Flight Center, SBIR Phase I Final Technical Rept. NASA/MSFC Contract NAS8-40679, Huntsville, AL, August 1996.
[10]Knuth, W. H., Chiaverini, M. J., Sauer, J. A., and Gramer, D. J., "Solid-Fuel Regression Rate Behavior of Vortex Hybrid Rocket Engines," *Journal of Propulsion and Power,* Vol. 18, No. 3, 2002, pp. 600-609.
[11]Knuth, W. H., Chiaverini, M. J., Gramer, D. J., and Sauer, J. A., "Final Report on Vortex Combustion Ramjet- a Phase I SBIR Project," Orbital Technological Corporation, NASA Contract No. NAS3-99039 Rept. OTC-GS075-FR-99-1, June 1999.
[12]Bloor, M. I. G., and Ingham, D. B., "The Flow in Industrial Cyclones," *Journal of Fluid Mechanics,* Vol. 178, 1987, pp. 507-519.
[13]Casalis, G., Avalon, G., and Pineau, J.-P., "Spatial Instability of Planar Channel Flow with Fluid Injection through Porous Walls," *The Physics of Fluids,* Vol. 10, No. 10, 1998, pp. 2558-2568.
[14]Griffond, J., Casalis, G., and Pineau, J.-P., "Spatial Instability of Flow in a Semiinfinite Cylinder with Fluid Injection through Its Porous Walls," *European Journal of Mechanics B/Fluids,* Vol. 19, No. 1, 2000, pp. 69-87.
[15]Griffond, J., and Casalis, G., "On the Nonparallel Stability of the Injection Induced Two-Dimensional Taylor Flow," *The Physics of Fluids,* Vol. 13, No. 6, 2001, pp. 1635-1644.
[16]Griffond, J., and Casalis, G., "On the Dependence on the Formulation of Some Nonparallel Stability Approaches Applied to the Taylor Flow," *The Physics of Fluids,* Vol. 12, No. 2, 2000, pp. 466-468.
[17]Ugurtas, B., Avalon, G., Lupoglazoff, N., Vuillot, F., and Casalis, G., "Stability and Acoustic Resonance of Internal Flows Generated by Side Injection," *Solid Propellant Chemistry, Combustion, and Motor Interior Ballistics*, Vol. 185, edited by V. Yang, T. B. Brill, and W.-Z. Ren, AIAA Progress in Astronautics and Aeronautics, Washington, DC, 2000, pp. 823-836.
[18]Ugurtas, B., Avalon, G., Lupoglazoff, N., and Vuillot, F., "Numerical Computations of Hydrodynamic Instabilities inside Channels with Wall Injection," AIAA Paper 99-2505, June 1999.
[19]Varapaev, V. N., and Yagodkin, V. I., "Flow Stability in a Channel with Porous Walls," *Fluid Dynamics (Izvestiya Akademii Nauk SSSR, Meckanika Zhidkosti i Gaza),* Vol. 4, No. 5, 1969, pp. 91-95.
[20]Herbert, T., "Parabolized Stability Equations," *Annual Review of Fluid Mechanics,* Vol. 29, 1997, pp. 245-283.
[21]Bertolotti, F. P., "Nonlinear Analysis of Boundary Layers with Streamwise Varying Properties," NASA Glenn, Annual Rept. NASA Training Grant NGT 50259, Columbus, OH, August 1989.
[22]Majdalani, J., and Vyas, A. B., "Inviscid Models of the Classic Hybrid Rocket," AIAA Paper 2004-3474, July 2004.
[23]Culick, F. E. C., "Rotational Axisymmetric Mean Flow and Damping of Acoustic Waves in a Solid Propellant Rocket," *AIAA Journal,* Vol. 4, No. 8, 1966, pp. 1462-1464.
[24]Don, W. S., and Solomonoff, A., "A Boundary Value Problem with Multiple Solutions from the Theory of Laminar Flow," *SIAM Journal on Scientific Computing,* Vol. 16, No. 6, 1995, pp. 1253-1268.
[25]Abu-Irshaid, E. M., Majdalani, J., and Casalis, G., "Stability of Rockets with Headwall Injection," AIAA Paper 2005-3543, July 2005.